Available online at www.sciencedirect.com

SciVerse ScienceDirect

Ceramics International 39 (2013) 1143–1152

CERAMICS INTERNATIONAL

www.elsevier.com/locate/ceramint

DC and *AC* susceptibility study of sol–gel synthesized $Bi_2Sr_2CaCu_2O_{8+\delta}$ superconductor

Devina Sharma[a,b,*], Ranjan Kumar[b], V.P.S. Awana[a]

[a]*National Physical Laboratory, Dr. K.S. Krishnan Marg, New Delhi 110012, India*
[b]*Department of Physics, Panjab University, Chandigarh 160014, India*

Received 3 July 2012; received in revised form 4 July 2012; accepted 10 July 2012
Available online 20 July 2012

Abstract

We study *DC* susceptibility along with amplitude and frequency dependence of *AC* susceptibility of sol–gel synthesized polycrystalline samples of $Bi_2Sr_2CaCu_2O_{8+\delta}$ (Bi-2212) sintered at different temperatures. In particular, it is demonstrated that susceptibility techniques are an effective tool to characterize granular characteristics of high temperature superconductors. The results are discussed in the framework of Bean's critical state model whence the field and temperature dependence of critical current density is determined. Flux pinning force density is calculated and possibility of the pinning mechanisms prevalent in type II superconductors are investigated. Flux creep activation energy is determined in the light of vortex dynamics exhibited by frequency dependence of *AC* susceptibility. Since polycrystalline samples are granular in nature, we calculated grain volume fraction and separated the contribution of grain and matrix susceptibility from total measured *AC* susceptibility. We establish that increase in the sintering temperature not only changes the grain morphology but affects the superconducting properties significantly, validating the impact of grain boundaries on superconducting performance of studied Bi-2212 superconductor.

Keywords: A. Sol–gel processes; C. Superconductivity; C. Magnetic properties

1. Introduction

The discovery of superconductivity in cuprate superconductors [1,2] opened a window of hope for their applications at easily accessible temperatures, i.e., above liquid nitrogen temperature of 77 K. However, in their polycrystalline samples, the grain boundaries acting as weak links due to small coherence length impeded the idea. In a want of replacing conventional type I superconductors like Nb–Ti and Nb_3Sn, new classes of materials like di-borides [3] and pnictides [4] have been discovered. Despite of it, cuprates are still the best potential candidates for large scale applications in view of their high critical temperature (above 77 K) and critical magnetic field (above 200 T) values among all known classes of superconductors. Granularity being a hindrance in the realization of their applications, if studied in a systematic way, can help in optimizing the superconducting properties of bulk polycrystalline tapes and wires. There have been constant efforts in this direction based on both experimental [5–7] as well as theoretical approach [8]. The effect of granularity/morphology on the superconducting properties of bulk polycrystalline samples is thus, among one of the greatest challenges in realizing applications of high temperature cuprate superconductors.

As far as the effect of granularity on bulk superconductivity is concerned, the same is best studied by magnetization than the electrical transport measurements. Since the inception of superconductivity [9], it took almost 22 years with the discovery of "Meissner effect", to reveal that superconductors possess unique properties [10] which cannot be explained by simply considering the infinite conductivity aspect. This led to the development of *DC* and *AC* mutual induction techniques for the characterization of superconductors [11]. Magnetic measurements are

*Corresponding author at: National Physical Laboratory, Dr. K.S. Krishnan Marg, New Delhi 110012, India.
Tel.: +91 11 45609357; fax: +91 11 45609310.
E-mail addresses: s.sharmadevina@gmail.com (D. Sharma), awana@mail.nplindia.ernet.in (V.P.S. Awana).
URL: http://www.freewebs.com/vpsawana (V.P.S. Awana).

0272-8842/$ - see front matter © 2012 Elsevier Ltd and Techna Group S.r.l. All rights reserved.
http://dx.doi.org/10.1016/j.ceramint.2012.07.038

preferred over transport measurements in case of superconductors for their various advantages over the later. They are considered as a non-destructive technique as no electrical contacts are required and the sample can be very small and even in the powder form. Also, they can be used to characterize the superconductor below its critical temperature (T_c), where resistivity tends to zero as measuring resistivity on lower limits is a challenge. Moreover, in case of granular superconductors like $Bi_2Sr_2Ca_{n-1}Cu_nO_{2n+4+\delta}$ ($n=1,2,3$), coupling of the superconducting grains have more pronounced effect on the magnetic properties over electrical properties, as there is a larger change in the shielding volume during coupling of the gains than the change in the resistivity due to coupling component of the conduction path.

Magnetic properties can be measured in either *AC* or *DC* field, by measuring the magnetic flux variation due to the magnetization of the sample. In case of *DC* magnetization, the sample is magnetized by a constant magnetic field and the magnetic moment induced is measured by induction technique, thus producing *DC* magnetization curves. Whereas in case of *AC* field magnetization, induced sample moment obtained is time dependent and hence is more informative. In high temperature superconductors (HTSc), *AC* susceptibility is a powerful tool to study vortex dynamics as this technique facilitates the study of change in vortex dynamics by varying amplitude and frequency of *AC* field, temperature and *DC* bias field. At higher field frequencies, due to time lag between the driving field and the induced magnetization, the obtained *AC* susceptibility (χ) consists of two components [11,12]; the in phase or real component (χ') and the out of phase or imaginary component (χ''). In case of superconductors, the real part of susceptibility depicts diamagnetic shielding of the sample, while imaginary part indicates the hysteric losses due to vortex motion. In granular superconductors, the two step transition in real part (χ') below T_c depicts diamagnetic shielding currents in intra- and inter-granular superconducting region respectively. Also, the appearance of two peaks in the imaginary part (χ'') at temperatures, T_P^{intra} and T_P^{inter} ($T_P^{intra} > T_P^{inter}$) indicates maximum hysteresis loss due to motion of intra-granular (Arbikosov) and inter-granular (Josephson) vortices [13] respectively. Maximum loss takes place when the magnetic flux lines penetrate up to the center of the sample and is indicated by the peak in imaginary part of susceptibility curve at a particular temperature called as peak temperature (T_p). When either the amplitude or the frequency of the driving field is changed, T_p shifts towards lower or higher temperature value respectively [14–16]. This peak shift is related to the pinning force density as per flux creep model given by Tinkham and Lobb [17] and Muller [13]. When frequency is increased, inter/intra-granular vortices have less time to relax and then penetrate the superconductor during each cycle of driving field. Therefore, in order to reach the full penetration, the effective inter-granular pinning force density must be weak. Since the strength of the pinning force density is inversely proportional to temperature, the peak temperature (T_P^{inter}/T_P^{intra}) shifts to higher value when frequency is increased. On the other hand, as the driving field amplitude increases, larger screening currents are required to shield the applied field. For this, strength of the pinning force density must be large, which in turn results in the shifting of peak (T_P^{inter}/T_P^{intra}) to the lower temperature with increasing field amplitude.

In the present work, we report the detailed analysis of *DC* and *AC* susceptibility measurements carried out for $Bi_2Sr_2CaCu_2O_{8+\delta}$ superconducting samples synthesized by sol–gel technique and sintered at various temperatures. Various superconducting parameters like critical temperature (T_c), upper critical field (H_{c2}), coherence length (ξ), temperature and field dependence of critical current density (J_c), flux pinning force density (F_P), flux creep activation energy (E_a), grain volume fraction (f_g), nature of weak links for susceptibility of superconducting grains (χ_g) and non-superconducting matrix (χ_m) are obtained for all the samples from these studies. Our work is an in-depth investigation of the effect of synthesis temperature on superconducting properties and various related mechanisms involved via *DC*/*AC* susceptibility study. We find that change in synthesis temperature effectively controlled the grains morphology and thus the grains coupling and hence the superconducting properties.

2. Experimental

Samples of $Bi_2Sr_2CaCu_2O_{8+\delta}$ superconductor were synthesized using sol–gel [18] method. High purity Bi_2O_3, $SrCO_3$, $CaCO_3$ and CuO were dissolved in nitric acid to obtain the nitrates of Bi, Sr, Ca and Cu. Direct use of various nitrates were avoided as they are hygroscopic in nature, thus making stoichiometry of the final product difficult to control as heating either removes water or decomposes the salt. The obtained solutions of nitrates were mixed and added to an aqueous solution of ethylene-diamene-tetra-acetic acid (EDTA). The molar ratio of EDTA acid to the total metal cation concentration was chosen to be unity. The pH of the obtained acidic solution was raised to seven by subsequently adding ammonium hydroxide to it. The liquid was stirred and heated continuously at 80 °C to result in a transparent viscous gel. On further heating the viscous gel transforms to foam like, and was finally converted into precursor powder. Obtained precursor powder was calcined at 500 °C to remove organic impurities. Further, the calcined powder was sintered at different temperatures viz. at 760, 780 and 820 °C to obtain three different samples of varying granular characteristics.

Phase analysis of the samples was done using Rigaku X-ray diffractometer. Scanning electron microscopy (SEM) technique was used for microstructural examination of the samples. Resistivity measurements were carried out using standard four probe technique using Physical

Property Measurement System (PPMS) of Quantum Design. The temperature dependent *DC* and *AC* measurements were done out using ACMS facility being employed in PPMS. The magnetic measurements were carried out for the samples in the temperature range of 10–110 K with amplitude and frequency of applied field varying from 0 to 9 Oe and 333 to 6666 Hz respectively.

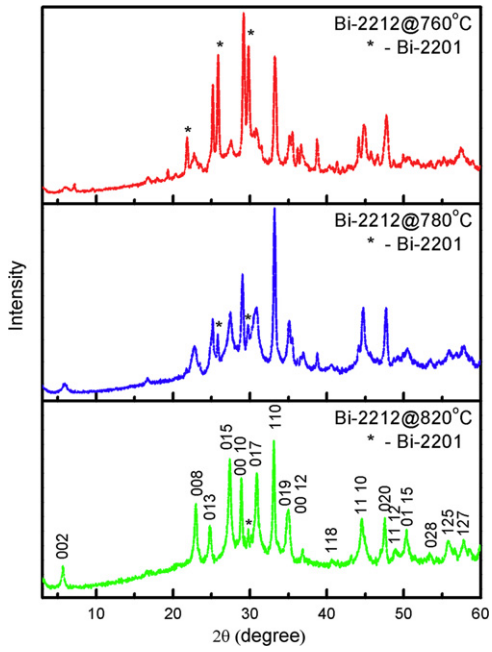

Fig. 1. XRD pattern of Bi-2212 samples sintered at 760, 780 and 820 °C.

3. Results and discussion

3.1. Microstructural studies

Fig. 1 shows the X-ray diffraction (XRD) pattern of the $Bi_2Sr_2CaCu_2O_{8+\delta}$ samples sintered at 760, 780 and 820 °C. The use of sol–gel synthesis technique facilitated the desired phase formation at temperatures as low as 760 °C to as high as 820 °C, which are considerably lower than that required in conventional solid state route. Although in BSCCO systems, the intergrowth of its various phases viz. 2201, 2212 and 2223 is abundant, but in our samples the major phase formed is of Bi-2212 with very few 2201 peaks. Moreover, the sharpness of the XRD peaks increase as the sintering temperature of the sample increases. This indicates increase of crystallite size with sintering temperature. Fig. 2 shows the SEM images of the samples sintered at different temperatures at same magnification of 5KX. Although the sintering temperature difference for the three samples is of only few degree Celsius (60 °C), but the morphology within this small temperature range has varied widely. From SEM images, it can be seen that the sample sintered at lowest temperature (760 °C) is quite porous with very small sized grains weakly connected to each other. But the sample sintered at 20 °C higher

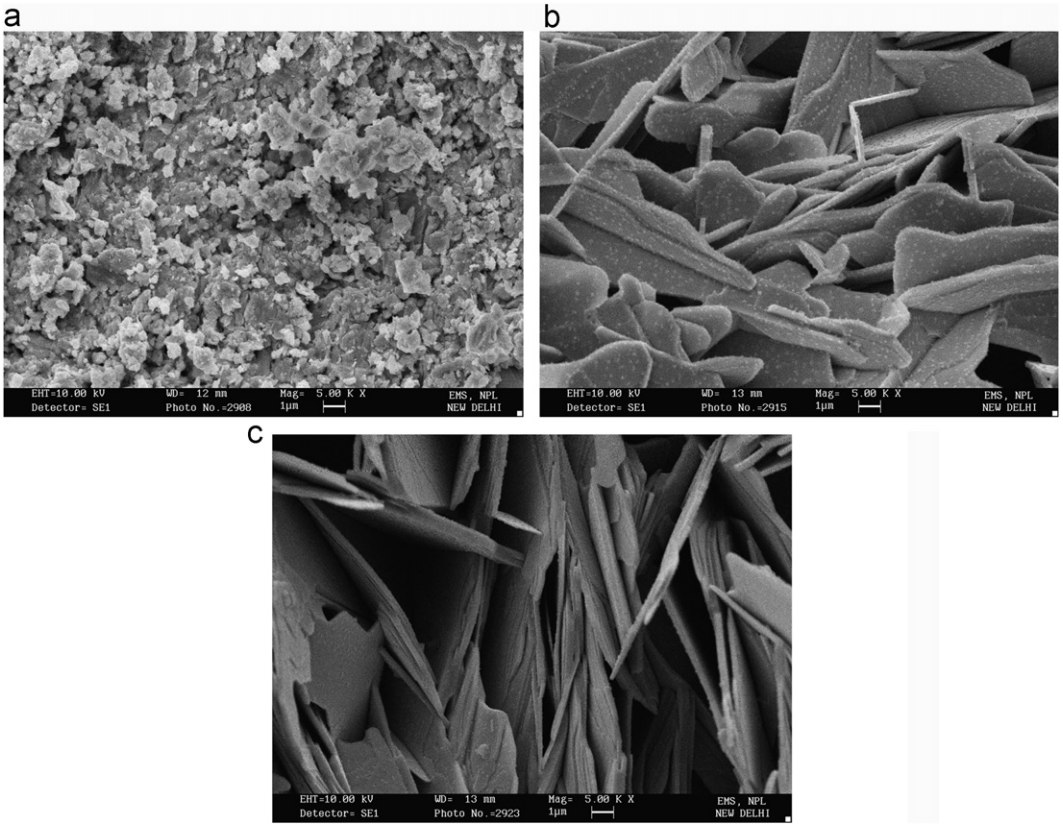

Fig. 2. SEM images of the samples sintered at (a) 760 (b) 780 and (c) 820 °C at 5KX magnification.

temperature (i.e. at 780 °C) the grain structure changes completely consisting of thin flakes with length and width of few μm. The density of the sample further improves on sintering at 820 °C. It is obvious from these SEM micrographs and XRD pattern, that there is a significant improvement in the grain morphology of the samples with rising sintering temperature, while superconducting Bi-2212 phase is yet mostly preserved in major amount.

3.2. Resistivity measurements

Fig. 3 shows the temperature dependence of resistivity for the three samples under investigation. It is clearly evident that the onset of the superconducting transition (T_c^{onset}) is nearly same for all the samples but the zero resistivity superconducting temperature ($T_c^{R=0}$) increases as the sintering temperature of the samples is increased. The superconducting transition width ($T_c^{onset} - T_c^{R=0}$) is increased significantly with decreasing sintering temperature. Also, the superconducting transition for 760 °C sintered sample is of two step nature, marking weaker coupling due to significant granularity in the sample. The transition becomes steeper for higher temperature sintered samples. The superconducting parameters obtained viz. T_c^{onset}, $T_c^{R=0}$ and $\Delta T_c = T_c^{onset} - T_c^{R=0}$ are tabulated in Table 1. The normal state resistivity of the granular superconducting sample is given by

$$\rho_n(T) = \alpha + \beta T \quad (1)$$

is contributed by the resistivity due to grains and grain boundaries. The former component is temperature independent, while the later is dependent on temperature. Therefore, the inter-grain coupling parameter at absolute zero temperature is given by the intercept (α) of Eq. (1) on *Y*-axis (as shown in Fig. 3). The value of α (see Table 1) decreases with increase in sintering temperature, indicating better inter-grain connectivity.

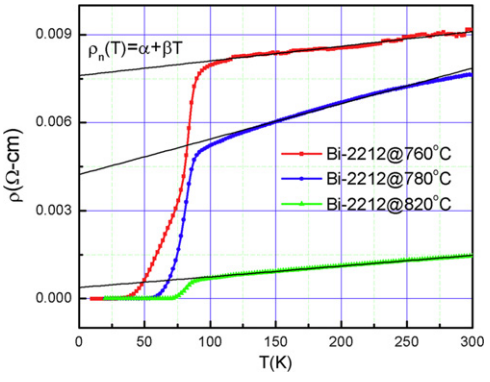

Fig. 3. Temperature dependence of resistivity for the three samples in the temperature range of 10–300 K.

Table 1
Various superconducting parameters extracted from resistivity measurements.

Sintering temperature (°C)	T_c^{onset} (K)	$T_c^{R=0}$ (K)	ΔT_c (K)	α	$\mu_o H_{C2}(T)$ at 0 K	ξ(0) (nm)
760	89.75	31.74	58.01	7.6×10^{-3}	56.9	2.4
780	89.80	49.78	40.02	4.2×10^{-3}	67.6	2.2
820	89.80	67.80	22.00	3.8×10^{-4}	136.3	1.6

Fig. 4 shows the temperature dependence of resistivity at various fields. The temperature dependence of upper critical field ($\mu_o H_{c2}$) estimated from 90% of $\rho(T,H)$ is shown in the inset of Fig. 5. Conventional single band WHH theory [14,19,20] which describes the orbital limited upper critical field of dirty type II superconductors is used to fit the obtained data using equations,

$$\ln(1/t) = \Psi(1/2 + \hbar/2t) - \Psi(1/2) \quad (2)$$

where, $t = T/T_c$, Ψ is a digamma function and ħ is given by

$$\hbar = 4H_{c2}/\pi^2 T_c(-dH_{c2}/dT)_{T=Tc}. \quad (3)$$

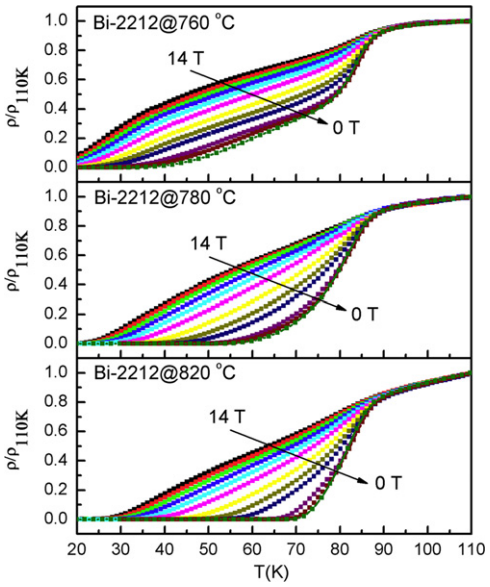

Fig. 4. Temperature dependence of normalized resistivity in the magnetic field range of 0–14 T.

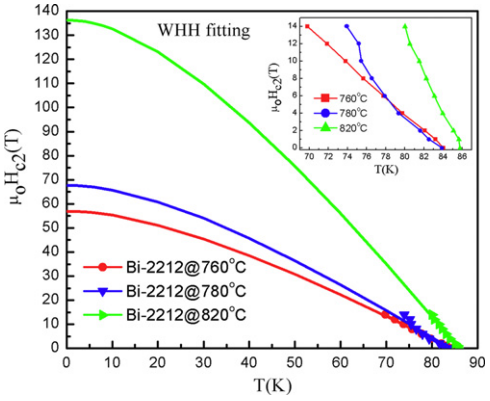

Fig. 5. Temperature dependence of upper critical field (symbols) and its fitting (solid line) using simplified WHH theory. Inset shows the corresponding experimental $\mu_o H_{c2}(T)$ derived from magneto-resistive transitions.

Fig. 5 shows the $\mu_o H_{c2}(T)$ of the three samples determined from 90% of $\rho_n(T)$ and its fitting using simplified WWH formula by symbols and solid lines respectively. The value of $\mu_o H_{c2}$ at absolute zero temperature determined using WHH fitting is consistent with earlier reports [21,22] and is found to increase with sintering temperature. The zero temperature coherence length $\xi(0)$ is estimated from $\mu_o H_{c2}(0)$ using the Ginzburg–Landau formula [14,20] given by $\mu_o H_{c2}(0) = \varphi_o/[2\pi\ \xi^2(0)]$, where, φ_o is flux quanta and given by 2.07×10^{-15} Wb. All the obtained parameters are listed in Table 1.

3.3. DC susceptibility studies

Fig. 6 shows the temperature dependence of *DC* magnetic susceptibility ($\chi_{dc}(T)$) for all the samples at an applied field of 10 Oe. The behavior of both, flux exclusion or zero field cooling (*ZFC*) and flux expulsion or field cooling (*FC*) is easily distinguishable for the three samples. For ideally pure superconductors, *ZFC* susceptibility, $\chi_{ZFC} = -1$. But, since real polycrystalline sample consists of superconducting grains embedded in a non-superconducting matrix [23], total χ is given by the summation of χ for superconducting region (i.e. $\chi_{SC} = -1$) and that for non-superconducting region (i.e. $\chi_{NSC} = 0$). So, the effective $\chi(\chi = \chi_{SC} + \chi_{NSC})$ is less than one. In the present case for the three samples the trend that χ_{ZFC} follows is: ${\chi_{ZFC}}^{820C} > {\chi_{ZFC}}^{780C} > {\chi_{ZFC}}^{760C}$. This in itself indicates that in these samples, the presence of non-superconducting region also follows the same trend of depreciation with increase of sintering temperature. In case of *FC*, $\chi = \chi_{SC} + \chi_{NSC}$, is lesser due to an added contribution because of flux, which is pinned due to the presence of defects in real polycrystalline samples, so as $\chi_{FC} < \chi_{ZFC}$. Thus, difference between the two susceptibilities given by $(\chi_{FC} - \chi_{ZFC})$ and is a measure of flux pinning in the sample. Therefore, in our case as is visible (opening of *FC* and *ZFC* transitions) from Fig. 6, flux pinning in the samples increases with the sintering temperature and is substantially high for the highest temperature sintered sample.

Fig. 7 shows *DC* magnetization curves as a function of applied field ($M(H)$ curves) at 5 K for the studied samples. Bean's critical state model [24] is used to determine critical current density (J_c) from these curves. As per above stated model, J_c of an infinitely long sample with rectangular cross section ($a \times b$) (with $a < b$) is obtained from the width ΔM of the $M(H)$ hysteresis loop using expression, $J_c(H) = [20 \times \Delta M(H)]/[a(1 - a/3b)]$ [25,26]. Fig. 8 shows the field dependence of J_c obtained from *DC* magnetization data. As expected in case of HTSc, there is a sudden characteristic drop in J_c at high magnetic fields. Obtained values of J_c (at zero field) for the three samples are tabulated in Table 2 and are consistent with earlier reports [27]. Clearly, there is a systematic increase in J_c with increase in sintering temperature. It is interesting to find that J_c increases almost four times for the sample, which is sintered only at 60 °C higher temperature than the sample sintered at lowest temperature (780 °C), indicating substantial improvement in the flux pinning. Marked improvement in J_c with sintering temperature shows the impact of grain morphology on the superconducting performance of polycrystalline HTSc.

In order to obtain deeper insight into the origin of improved pinning properties with sintering temperature, an extended analysis of pinning force density is carried out. Inset of Fig. 8 shows the flux pinning density given by, $F_P = J_c \times B$ for the three samples at 5 K. Clearly there is substantial increase in the maximum pinning force (F_{Pmax})

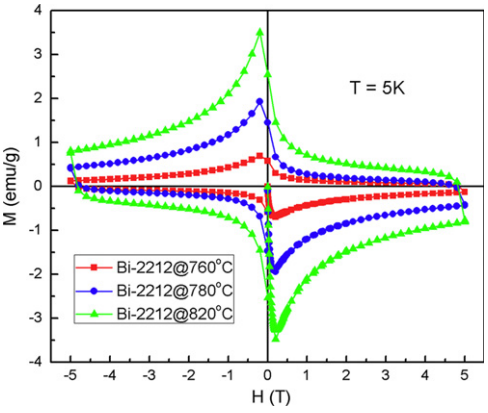

Fig. 7. Field dependence of *DC* magnetization at 5 K temperature.

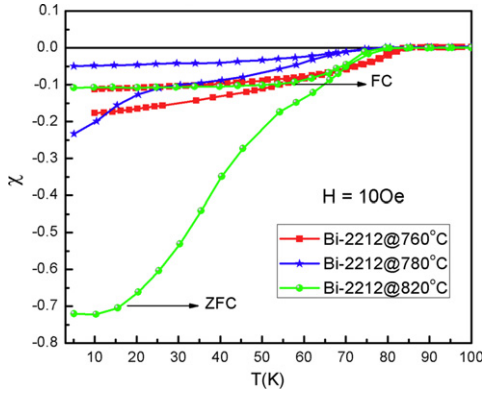

Fig. 6. Temperature dependence of *DC* susceptibility at an applied field of 10 Oe.

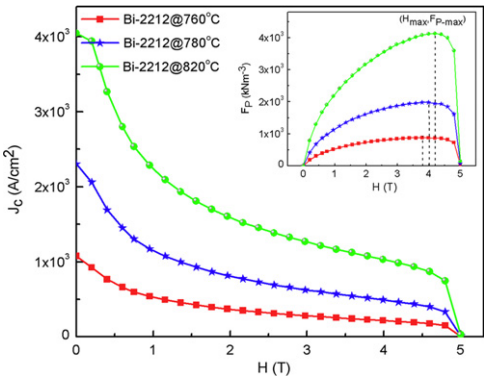

Fig. 8. Field dependence of critical current density for various samples at 5 K temperature. Inset shows field dependence of flux pinning density.

Table 2
Various superconducting parameters extracted from *DC* and *AC* susceptibility measurements.

Sintering temperature (°C)	From *DC* susceptibility		From *AC* susceptibility			
	J_c (Acm^{-2}) at 5 K, 0 T	F_{p-max} (N/m^3)	E_a (K)	J_c (Acm^{-2}) at 0 K, 10 Oe	n	f_g
760	1.08×10^3	0.8×10^6	–	–	–	0.012
780	2.30×10^3	2.0×10^6	1914.08	0.15×10^3	1.9	0.017
820	4.05×10^3	4.0×10^6	5629.60	1.33×10^3	2.4	0.071

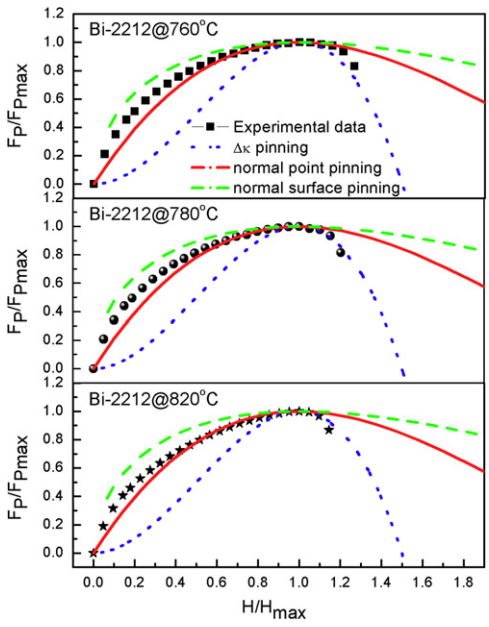

Fig. 9. Normalized pinning force as a function of normalized field. Doted (blue), solid (red) and dashed (green) line represents theoretical curves given by Eqs. (4)–(6) respectively. (For interpretation of the references to color in this figure legend and the corresponding text, the reader is referred to the web version of this article.)

with increased sintering temperature. Also, the corresponding field (H_{max}) shifts to higher value. This again shows improvement in flux pinning with sintering temperature, which corroborates with the results obtained from $\chi_{dc}(T)$ curves. Further, to probe into flux pinning mechanism, normalized pinning force density, $f_P=F_P/F_{Pmax}$ is plotted against normalized field, $b=H/H_{max}$. According to Dew Huges [28], flux pinning force in type II superconductors is influenced by superconducting nature and size of pinning centers, microstructure wavelength and flux lattice rigidity. For high temperature superconductors, the scaling of f_P-b is often analyzed using three theoretical models [28–32]:

$$f_P(b) = 3b^2(1-2b/3); \quad \text{for } \Delta\kappa \text{ pinning}, \tag{4}$$

$$f_P(b) = 9/4b(1-b/3)^2; \quad \text{for normal point pinning}, \tag{5}$$

$$f_P(b) = 25/16b^{-1/2}(1-b/5)^2; \quad \text{for normal surface pinning}, \tag{6}$$

Fig. 9 shows the scaling of the f_P-b curves for the three samples. Theoretical curves for Eqs. (1)–(3) are represented in the figure by a doted (blue), solid (red) and dashed (green) line respectively. For fields below H_{max}, data points for the three samples scale between normal point pinning and surface pinning. At higher fields, we note a crossover to the $\Delta\kappa$ pinning mechanism in all the three samples. However, because the data above H_{max} are limited only, hence one cannot conclude the presence of $\Delta\kappa$ pinning with certainty. Therefore, from the critical current density and flux pinning analysis, it is clear that, though the flux pinning mechanism (i.e. normal pinning) or the nature of pinning centers is identical for samples sintered at various temperatures but there is a substantial improvement in J_c and F_P.

3.4. AC susceptibility studies

Fig. 10(a) and (b) shows the temperature dependence of the real and imaginary component of *AC* susceptibility (*ACS*) for the three different temperature sintered samples in the field ranging from 0.5 to 9 Oe. In polycrystalline HTSc, a typical feature of *ACS* is the appearance of two drops in χ' accompanied by two peaks in χ'' [25]. In Fig. 10(a), double drop in the χ' for all the three samples is clearly seen but the same is materialized differently in three of them. Saturation in the diamagnetic signal with temperature is clearly visible for the highest temperature sintered sample (820 °C) but it is absent in the other samples. This shows increasing diamagnetic volume fraction with improved morphology for the samples being sintered at higher temperature. Fig. 10(b) shows the temperature dependence of imaginary part of *AC* susceptibility at various field amplitudes. In case of sample sintered at 760 °C, dissipative peak corresponding to intra-granular losses is clearly visible around T_c^{onset} but, the peak corresponding to inter-granular losses is not visible as it is below minimum temperature measurement range. Wide separation of inter- and intra-granular loss peaks shows poor coupling between the grains. For a little higher sintering temperature of 780 °C, inter-granular peak is feebly visible and shifts to higher temperature as compared to the sample sintered at 760 °C, with a very weak intra-granular loss peak (see inset of Fig. 10(b)). Inter- and intra-granular peak separation has noticeably decreased, which shows improvement in grain coupling. In contrast, for the sample sintered at highest temperature

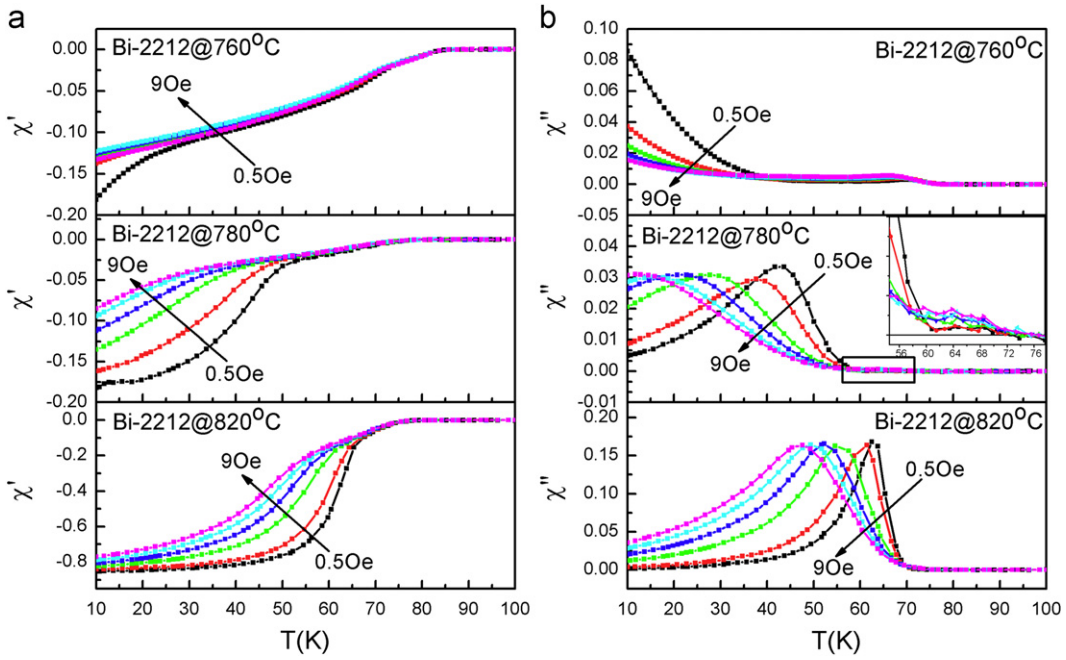

Fig. 10. (a) Temperature dependence of real component of *AC* susceptibility for various samples in the applied field ranging from 0.5 to 9 Oe with frequency of 333 Hz. (b) Temperature dependence of imaginary component of *AC* susceptibility for various samples in the applied field ranging from 0.5 to 9 Oe with frequency of 333 Hz. Inset in the middle figure shows the enlarged view of intra-granular loss peaks highlighted in the same figure with rectangular box.

(820 °C), only one loss peak is observed, which is relatively at quite high temperature than others. Appearance of a single dissipation peak seems to be because of merging of closely located inter- and intra-granular loss peaks, which signifies best coupling of gains for sintering temperature of 840 °C among all the studied samples. Hence, on comparing χ'' of the three samples, there are two important observations. First, we find that inter-granular loss peaks shift to higher temperature and second, they become sharper for samples sintered at higher temperature indicating improvement in flux pinning and grain coupling respectively with sintering temperature. The improvement in grain coupling and flux pinning with sintering temperature demonstrated by *ACS* curves is in corroboration with those being obtained from $\chi_{dc}(T)$ (Section 3.3) and normal state resistivity (Section 3.2) analysis respectively. Also, it is interesting to see in Fig. 10(b), that with increase in the applied field amplitude, the loss peak shifts to lower temperature as expected (explained above), but to different extent for samples sintered at 780 and 820 °C (loss peak of 760 °C sintered sample is invisible being below minimum measured temperature range). It is well known that when applied field reaches at the center of the sample, losses become maximum i.e. at the peak temperature (T_p) of χ'', applied field can be considered as full penetration field (H^*). Therefore temperature dependence of critical current density $J_c(T)$ can be estimated using Bean's model [24]. According to the stated model, critical current density at peak temperature (T_p) of *AC* susceptibility can be

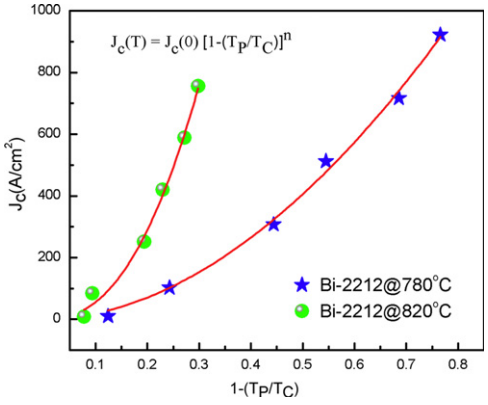

Fig. 11. Temperature dependence of critical current density (symbols) and its fitted curve (solid line) as per equation, $J_c=J_c(0)(1-T_P/T_C)^n$ for sample sintered at 780 and 820 °C.

written as

$$J_c(T_p) = H^*/\sqrt{ab} \tag{7}$$

for rectangular bar shaped sample of cross section $2a \times 2b$. Inter-granular current density obtained using Eq. (7) is presented in Fig. 11 with filled square symbols for samples sintered at 780 and 820 °C. The temperature dependence of J_c is found to obey power law given by $J_c(T)=J_c(0)(1-T_p/T_c)^n$ [33,34], where, T_c is the zero resistivity critical temperature. Values of $J_c(0)$ and 'n' obtained from fit to experimental data are provided in Table 2. The obtained $J_c(0)$ values are higher for the sample sintered at 840 °C than

that at 780 °C and are of the same order as those obtained from *DC* susceptibility. It is well known that in polycrystalline granular superconductors, superconducting grains are separated by non-superconducting matrix, which strongly determines the temperature dependence of J_c. According to Ambegaokar and Baratoff [35], grain boundary regions in granular superconductors can be treated as superconducting-normal-superconducting (*SNS*) or superconducting-insulating-superconducting (*SIS*) junctions. De Gennes [36] showed that in case of *SNS* junctions, the value of '*n*' in $J_c(T)=J_c(0)(1-T_p/T_c)^n$ relation is 2 for T close to T_c. In our case '*n*' is nearly 2 for both the samples. Hence, irrespective of the sintering temperature nature of the weak links is of *SNS* type in both the samples.

Fig. 12 shows the frequency dependence of real and imaginary part of *AC* susceptibility of the three samples under investigation at 1 Oe with frequency in the range of 333–6666 Hz. Frequency change has very little effect on the susceptibility of the samples as compared to that of amplitude variation. Again, as expected (explained above), with increase in the frequency of the applied field, the dissipative peak shifts to higher temperature but the extent of shift is different for various samples. This shift in the loss peak indicates that flux creep influences inter-granular flux dynamics. Loss peak in χ'' appears when the measuring frequency is of the order of inverse relaxation time of vortex system [37]. Therefore, there is logarithmic dependence of peak position on *ac* field frequency. This dependence is used to determine the activation energy (E_a) for flux creep. For a particular frequency, the value of peak temperature is given by $f=f_o\exp(-E_a/k_BT)$ [38,39], where f_o is the attempt frequency and E_a is the activation energy of the flux creep. So, $E_a(H_{ac},T)$ for flux creep can be calculated from slope of the graph between log of

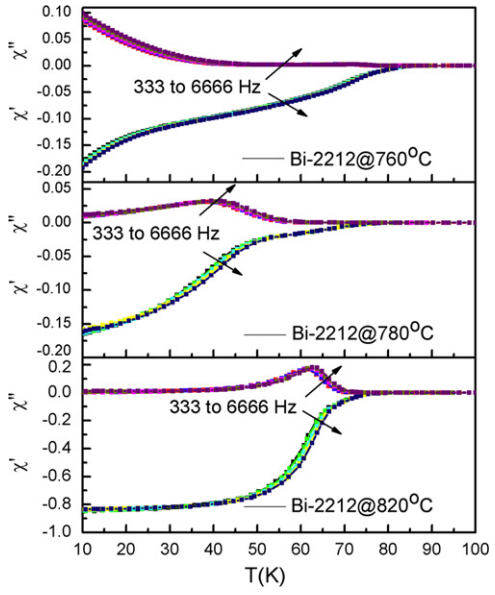

Fig. 12. Temperature dependence of real and imaginary component of *AC* susceptibility for various samples in the applied field of 1 Oe with frequency ranging from 333 to 6666 Hz.

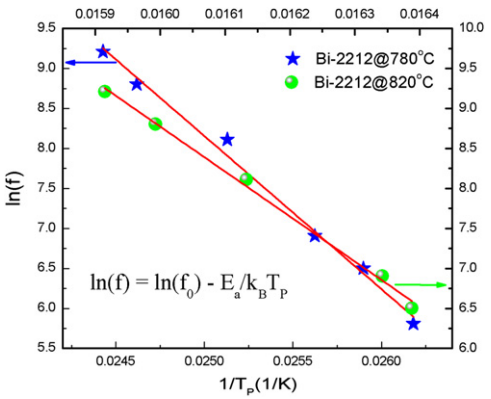

Fig. 13. Linear fitting curves (solid line) for ln(f) versus $1/T_P$ for samples sintered at 780 and 820 °C.

frequency and inverse of peak temperature ($1/T_P$). Fig. 13 shows plots for ln(f) versus ($1/T_P$) for samples sintered at 780 and 820 °C. E_a values obtained from the slope of the linear fitting of the curve (see Table 2), is found to be 1914.08 and 5629.60 K at 1 Oe field for samples sintered at 760 and 820 °C respectively. That is, the flux creep activation energy (E_a) is higher for samples sintered at higher temperature. This increase in E_a indicates that the flux lines are better pinned as sintering temperature is increased.

It is well known that granular superconductors are considered to consist of superconducting grains embedded in normal or poorly superconducting matrix or network. *AC* susceptibility techniques also allow determining the susceptibility of superconducting grains and non-superconducting matrix. According to the critical state model given by Chen et al.,[40] the complex susceptibility of the sample can be written as

$$\chi = f_g\chi_g + (1-f_g)\chi_m \tag{8}$$

where, χ_g and χ_m are the complex susceptibilities of superconducting grains and matrix respectively and f_g is the volume fraction of grains. Since, in *AC* susceptibility measurements, the field amplitude used is lower than the lower critical field of the sample, therefore χ_g can be taken as -1. Substituting, $\chi_g=-1$ in Eq. (8), the real and imaginary component of the susceptibility of the sample can be written as

$$\chi_m' = (\chi' + f_g)/(1-f_g) \tag{9}$$

$$\chi_m'' = \chi''/(1-f_g). \tag{10}$$

In order to determine χ_m, f_g has to be determined first. Chen et al. [41] determined f_g with elaborate method using critical state model of Kim et al. [42]. Celibi [43] used a simple Cole–Cole (χ' vs. χ'' plot) method to determine f_g and found it to be consistent with that obtained by Chen et al. Hence, we determined the value of f_g by plotting χ' versus χ'' as shown in Fig. 14. The extrapolated onset of

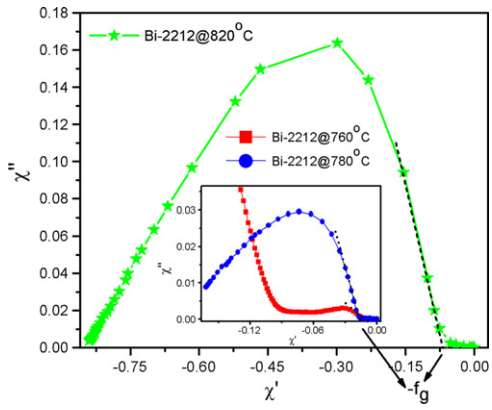

Fig. 14. $\chi'(\chi'')$ plot for sample sintered at 820 °C at a field of 1 Oe and 333 Hz. Inset shows $\chi'(\chi'')$ plots for samples sintered at 760 and 820 °C at the same field.

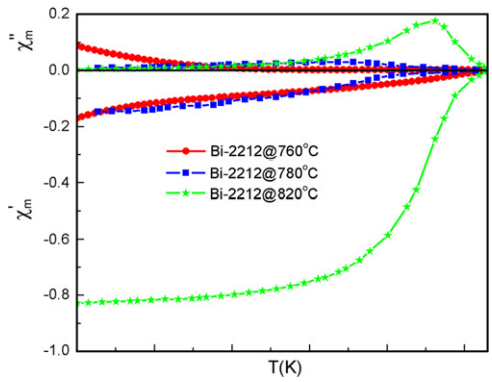

Fig. 15. Temperature dependence of matrix susceptibility where high temperature data corresponding to intra-granular contribution has been removed.

$\chi''(\chi')$ indicated by arrow in figure roughly shows the value of f_g of the samples sintered at various temperatures. We find that grain volume fraction (see Table 2) significantly increases for samples sintered at higher temperatures as can also be inferred from SEM images. Using the obtained values of f_g, $\chi'_m(T)$ and $\chi''_m(T)$ at 1 Oe and 333 Hz is extracted using Eqs. (9) and (10) and is shown in Fig. 15. It is to be noted that the high temperature data (78–110 K, 64–100 K and 70–100 K) corresponding to intra-granular contribution is removed in order to plot matrix susceptibility for each of the samples (sintered at 760, 780 and 820 °C) respectively. Similarly, grain susceptibility $\chi'_g(T)$ and $\chi''_g(T)$ is plotted in Fig. 16 using the following equations [44]:

$$\chi'_g = \chi'/f_g \tag{11}$$

$$\chi''_g = \chi''/f_g. \tag{12}$$

and removing low temperature data (10–77 K, 10–63 K and 10–69 K) corresponding to inter-granular contribution for each sample (sintered at 760, 780 and 820 °C) respectively.

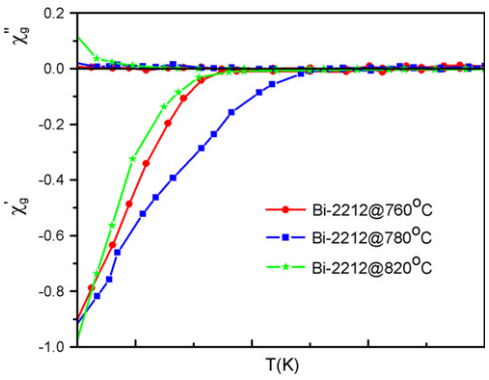

Fig. 16. Temperature dependence of grain susceptibility where low temperature data corresponding to inter-granular contribution has been removed.

4. Conclusion

Polycrystalline superconducting samples of $Bi_2Sr_2CaCu_2O_{8+\delta}$ were synthesized at various sintering temperatures using sol–gel technique and their detailed analysis of *AC* and *DC* susceptibility studies were carried out to unearth the importance of morphology in these materials. Temperature dependence of J_c was found to follow $J_c(T)=J_c(0)(1-T_p/T_c)^n$ equation with '*n*' nearly 2 for the investigated samples which shows *SNS* type behavior of the weak links in these samples. Flux pinning force density calculated from *DC* susceptibility data was found to increase with sintering temperature. Also, all the three samples were found to exhibit the same, normal pinning mechanism. Flux creep activation energy was found to increase for samples sintered at higher temperatures fortifying the fact of improved flux pinning. Enhancement in grain coupling with sintering temperature was evident from narrowing of loss peaks and resistivity transitions. We demonstrated that *AC* and *DC* susceptibility techniques are powerful tools to study wider aspects of superconductivity, in particular to investigate the role of superconducting grains and their coupling in bulk polycrystalline samples. The crux of this investigation is that with an increase in sintering temperature, there is a significant improvement grain morphology leading to enhancement of overall superconducting properties like T_c, J_c and F_P of $Bi_2Sr_2CaCu_2O_{8+\delta}$ bulk polycrystalline samples. The overall nature of the grain boundaries and flux pinning mechanism though remains same. Thus, cumulative sincere efforts towards science and engineering of grain boundary are very much required to unleash the potential of high temperature superconductors.

Acknowledgments

Authors thank Prof. R.C. Budhani, Director, NPL for his keen interest and encouragement for superconductivity research. Mr. A.K. Sood from NPL is acknowledged for providing us with the SEM micrographs.

References

[1] J.C. Bednorz, K.A. Müller, Possible high T_c superconductivity in Ba–La–Cu–O system, Zeitschrift für Physik B 64 (1986) 189.

[2] M.K. Wu, J.R. Ashburn, C.J. Torng, P.H. Hor, R.L. Meng, L. Gao, Z.J. Huang, Y.Q. Wang, C.W. Chu, Superconductivity at 93 K in a new mixed phase Y–Ba–Cu–O compound system at ambient pressure, Physical Review Letters 58 (1987) 908.

[3] Jun Nagamatsu, Norimasa Nakagawa, Takahiro Muranaka, Yuji Zenitani, Jun Akimitsu, Superconductivity at 39 K in magnesium diboride, Nature 410 (2001) 63.

[4] Y. Kamihara, T. Watanabe, M. Hirano, H. Hosono, Iron-based layered superconductor La[$O_{1-x}F_x$]FeAs (x=0.05–0.12) with T_c=26 K, Journal of the American Chemical Society 130 (2008) 3296.

[5] R.F. Klie, J.P. Buban, M. Varela, A. Franceschetti, C. Jooss, Y. Zhu, N.D. Browning, S.T. Pantelides, S.J. Pennycook, Enhanced current transport at grain boundaries in high-T_c superconductors, Nature 435 (2005) 475.

[6] G. Hammerl, H. Bielefeldt, S. Leitenmeier, A. Schmehl, C.W. Schneider, A. Weber, J. Mannhart, Large grain boundary area superconductors, European Physical Journal B 27 (2002) 299.

[7] D.C. van der Laan, T.J. Haugan, P.N. Barnes, Effect of compressive uniaxial strain on the critical current density of grain boundaries in superconducting YBa2Cu3$O_{7-\delta}$ films, Physical Review Letters 103 (2009) 027005.

[8] S. Graser, P.J. Hirschfeld, T. Kopp, R. Gutser, B.M. Andersen, J. Mannhart, How grain boundaries limit supercurrents in high-temperature superconductors, Nature Physics 6 (2010) 609.

[9] H. Kamerlingh Onnes, Further experiments with liquid helium. D. On the change of electric resistance of pure metals at very low temperatures, etc. V. The disappearance of the resistance of mercury, Communications from the Physical Laboratory at the University of Leiden, vol. 122b (1911).

[10] W. Meissner, R. Ochesenfeld, Ein neuer Effekt bei Eintritt der Supraleitfähigkeit, Naturwissenschaften 21 (1933) 787.

[11] R.B. Goldfarb, M. Lelental, C.A. Thomson, in: R.A. Hein, T.L. Francavilla, D.H. Liebenberg (Eds.), Magnetic Susceptibility of Superconductors and Other Spin Systems, Plenum Press, New York, 1991.

[12] R.B. Goldfarb, A.F. Clark, A.I. Braginski, A.J. Panson, Evidence for two superconducting components in oxygen-annealed single-phase Y–Ba–Cu–O, Cryogenics 27 (1987) 475.

[13] K.H. Muller, AC susceptibility of high temperature superconductors in a critical state model, Physica C 159 (1989) 717.

[14] N.P. Liyanawaduge, Shiva Kumar Singh, Anuj Kumar, Rajveer Jha, B.S.B. Karunarathne, V.P.S. Awana, Magnetisation and magneto resistance in Y($Ba_{1-x}Sr_x$)$_2Cu_3O_7$ (x=0.0–0.5) superconductor, Superconductor Science and Technology 25 (2012) 035017.

[15] N.P. Liyanawaduge, Shiva Kumar Singh, Anuj Kumar, V.P.S. Awana, H. Kishan, Superconducting and magnetic properties of Zn doped $YBa_2Cu_3O_7$, Journal of Superconductivity & Novel Magnetisim 24 (2011) 1599.

[16] G. Bonsignore, A. Agliolo Gallitto, M. Li Vigni, J.L. Luo, G.F. Chen, N.L. Wang, D.V. Shovkun, Intergrain effects in the AC susceptibility of polycrystalline $LaFeAsO_{0.94}F_{0.06}$, Journal of Low Temperature Physics 162 (2011) 40.

[17] M. Tinkham, C.J. Lobb, in: H. Ehrenreich, D. Turnbull (Eds.), Solid State Physics, vol. 42, Academic, San Diego, 1989.

[18] J. Fransaer, J.R. Roos, L. Delaey, O. Van Der Biest, O. Arkens, J.P. Celis, Sol–gel preparation of high-T_c Bi–Sr–Ca–Cu–O and Y–Ba–Cu–O superconductors, Journal of Applied Physics 65 (1989) 3277.

[19] N.R. Werthamer, E. Helfand E, P.C. Hohenberg, Temperature and purity dependence of the superconducting critical field, H_{c2}. III. Electron spin and spin–orbit effects, Physical Review 147 (1966) 295.

[20] Hechang Lei, C. Petrovic, Upper critical fields and superconducting anisotropy of $K_{0.70}Fe_{1.55}Se_{1.01}S_{0.99}$ and $K_{0.76}Fe_{1.61}Se_{0.96}S_{1.04}$ single crystals, European Physical Letters 95 (2011) 57006.

[21] G.C. Kim, M. Cheon, H. Kim, Y.C. Kim, D.Y. Jeong, Hole concentration dependence of penetration depth and upper critical field in Bi_2Sr_2(Ca,Y)$Cu_2O_{8+\delta}$ extracted from reversible magnetization, Physical Review B 72 (2005) 064525.

[22] Yoichi Ando, G.S. Boebinger, A. Passner, L.F. Schneemeyer, T. Kimura, M. Okuya, S. Watauchi, J. Shimoyama, K. Kishio, K. Tamasaku, N. Ichikawa, S. Uchida, Resistive upper critical fields and irreversibility lines of optimally doped high-T_c cuprates, Physical Review B 60 (1999) 12475.

[23] F. Gomory, Characterization of high-temperature superconductors by AC susceptibility measurements, Superconductor Science and Technology 10 (1997) 523.

[24] C.P. Bean, Magnetization of hard superconductors, Physical Review Letters 8 (1962) 250.

[25] G. Krabbes, G. Fuchs, W. Canders, H. May, R. Palka, High Temperature Superconductor Bulk Materials, Wiley-VCH, Weinheim, 2006.

[26] C.S. Yadav, P.L. Paulose, Upper critical field, lower critical field and critical current density of $FeTe_{0.60}Se_{0.40}$ single crystals, New Journal of Physics 11 (2009) 103046.

[27] V. Garnier, R. Caillard, A. Sotelo, G. Desgardin, Relationship among synthesis, microstructure and properties in sinter-forged Bi-2212 ceramics, Physica C 319 (1999) 197.

[28] D. Dew-Hughes, Flux pinning mechanisms in type II superconductors, Philosophical Magazine 30 (1974) 293.

[29] E.J. Kramer, Scaling laws for flux pinning in hard superconductors, Journal of Applied Physics 44 (1973) 1360.

[30] E.J. Kramer, A.D. Gupta, A model of surface flux line pinning in type II superconductors, Philosophical Magazine 26 (1972) 769.

[31] T. Higuchi, S.I. Yoo, M. Murakami, Comparative study of critical current densities and flux pinning among a flux-grown $NdBa_2Cu_3O_y$ single crystal, melt-textured Nd–Ba–Cu–O, and Y–Ba–Cu–O bulks, Physical Review B 59 (1999) 1514.

[32] Y. Ding, Y. Sun, J.C. Zhuang, L.J. Cui, Z.X. Shi, M.D. Sumption, M. Majoros, M.A. Susner, C.J. Covacs, G.Z. Li, E.W. Collings, Z.A. Ren, Density effect on critical current density and flux pinning properties of polycrystalline $SmFeAsO_{1-x}F_x$ superconductor, Superconductor Science and Technology 24 (2011) 125012.

[33] H. Salamati, P. Kameli, AC susceptibility study of YBCO thin film and BSCCO bulk superconductors, Journal of Magnetism and Magnetic Materials 278 (2004) 237.

[34] H. Salamati, P. Kameli, Effect of deoxygenation on the weak-link behavior of $YBa_2Cu_3O_{7-\delta}$ superconductors, Solid State Communications 125 (2003) 407.

[35] V. Ambegaokar, A. Baratoff, Tunneling between superconductors, Physical Review Letters 10 (1963) 486.

[36] P.G. De Gennes, Boundary effects in superconductors, Reviews of Modern Physics 36 (1964) 225.

[37] V.B. Geshkenbein, V.M. Vinokur, R. Fehrenbacher, ac absorption in the high-T_c superconductors: reinterpretation of the irreversibility line, Physical Review B 43 (1991) 3748.

[38] M. Nikolo, R.B. Goldfarb, Flux creep and activation energies at the grain boundaries of Y–Ba–Cu–O superconductors, Physical Review B 39 (1989) 6615.

[39] P.W. Anderson, Theory of flux creep in hard superconductors, Physical Review Letters 9 (1962) 309.

[40] D.X. Chen, Y. Mei, H.L. Luo, Critical-current density in sintered high-T_c (Bi, Pb)–Sr–Ca–Cu-Oxide, Physica C 167 (1990) 317.

[41] D.X. Chen, J. Nogues, K.V. Rao, A.c. susceptibility and intergranular critical current density of high T_c superconductors, Cryogenics 29 (1989) 800.

[42] Y.B. Kim, C.F. Hemstead, A.R. Strnad, Critical persistent currents in hard superconductors, Physical Review Letters 9 (1962) 306.

[43] S. Celibi, Comparative AC susceptibility analysis on Bi–(Pb)–Sr–Ca–Cu–O high-T_c superconductors, Physica C 316 (1999) 251.

[44] D.X. Chen, A. Sanchez, T. Puig, L.M. Martinez, J.S. Munoz, AC susceptibility of grains and matrix for high-T_c superconductors, Physica C 168 (1990) 652.